Aerodynamic Effects of Gurney Flaps
on the Rotor Blades of a Research Wind Turbine

Jörg Alber[1], Rodrigo Soto-Valle[1], Marinos Manolesos[2], Sirko Bartholomay[1], Christian Navid Nayeri[1], Marvin Schönlau[1], Christian Menzel[1], Christian Oliver Paschereit[1], Joachim Twele[3], Jens Fortmann[3]

5 [1] Technische Universität Berlin, Hermann-Föttinger Institut, Müller-Breslau-Str. 8, 10623 Berlin, Germany
[2] College of Engineering, Swansea University, Bay Campus, Fabian Way, Swansea, SA1 8EN, United Kingdom
[3] Hochschule für Technik und Wirtschaft Berlin, Wilhelminenhofstraße 75A, 12459 Berlin, Germany

*Correspondence to*: Joerg Alber (joerg.alber@htw-berlin.de)

Abstract.

10 This paper investigates the aerodynamic impact of Gurney flaps on a research wind turbine of the Hermann-Föttinger Institute at the Technische Universität Berlin. The rotor radius is 1.5 meters and the blade configurations consist of the clean and the tripped baseline cases emulating the effects of forced leading edge transition. The wind tunnel experiments include three operation points based on tip speed ratios of 3.0, 4.3 and 5.6, reaching Reynold numbers of approximately 250,000. The measurements are taken by means of three different methods; Ultrasonic Anemometry in the wake, surface pressure taps in the mid-span blade region and strain gauges at the blade root. The retrofit application consists of two Gurney flap heights of 0.5 % and 1.0 % in relation to the chord length, which are implemented perpendicular to the pressure side at the trailing edge. As a result, the Gurney flap configurations evoke performance improvements in terms of the axial wake velocities, the angles-of-attack and the lift coefficients. The enhancement of the root bending moments imply an increase of both the rotor torque and the thrust. Furthermore, the aerodynamic impact appears to be more pronounced in the tripped case compared to

20 the clean case. Gurney flaps are considered a worthwhile passive flow-control device in order to alleviate the adverse effects of early separation and leading edge erosion of horizontal axis wind turbines.

1 Introduction

The energy yield of modern Horizontal Axis Wind Turbines (HAWTs) is supposed to be optimal while keeping the maintenance costs as low as possible over a lifetime of around 20 years. However, the performance of rotor blades faces

25 serious challenges, two of which are early separation and roughness effects. Early separation is a problem especially in the inner blade region towards the root where the Angles-of-attack (AoA) are elevated due to structural constraints, such as limited chord-length as well as twist-angles, see Figure 1 (a). Over time, the resulting dynamic loads contribute to the material fatigue of the blade. At the same time, roughness effects are evoked by the longstanding surface erosion throughout the entire blade span, especially close to the Leading Edge (LE), see Figure 1 (b). Apart from the broad range of weather

30 conditions, surface roughening is aggravated by rain, insects as well as sand or salt particles. Consequently, the energy yield
    of HAWTs is often found lower than predicted or regressing over time (Wilox et al., 2017).

(a)   (b)
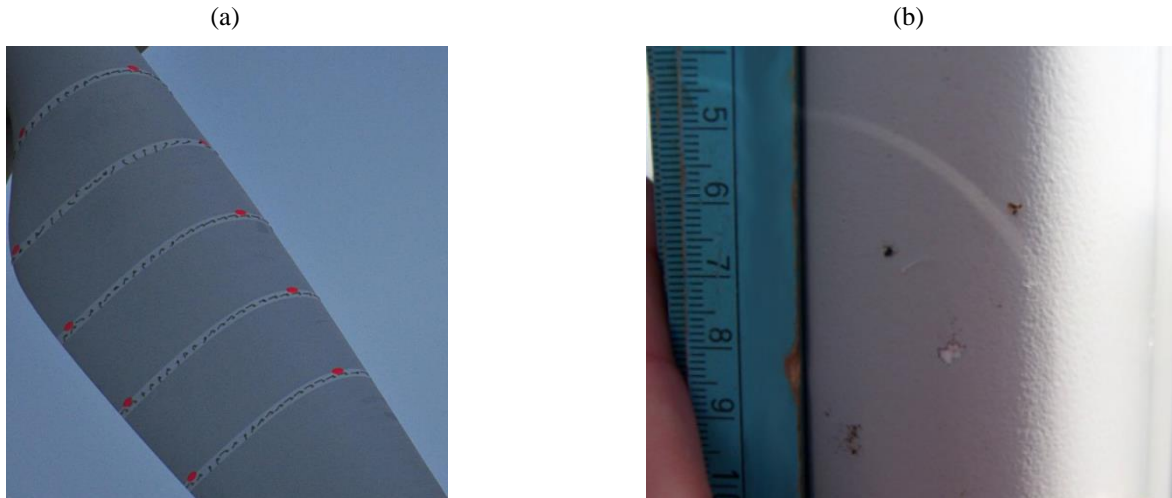
Figure 1. Rotor blades of utility scale wind turbines (a) Flow indicators to detect early separation in the root region, reproduced from
Pechlivanoglou et al. (2013). (b) Leading edge roughness, reproduced from Pechlivanoglou et al. (2010).

This paper investigates an approach to improve the aerodynamic performance of rotor blades; the retrofit application of
35 Gurney Flaps (GFs). This passive flow-control device consists of a wedge- or right-angle profile that is attached
    perpendicular to the pressure side at the Trailing Edge (TE). The GF-height, *GF*, in relation to the chord-length is the main
    aerodynamic parameter, shown in Figure 2 (a). It is usually in the range of 0.5 %c < *GF* < 2.0 %c without taking the TE
    thickness into account.

(a)   (b)
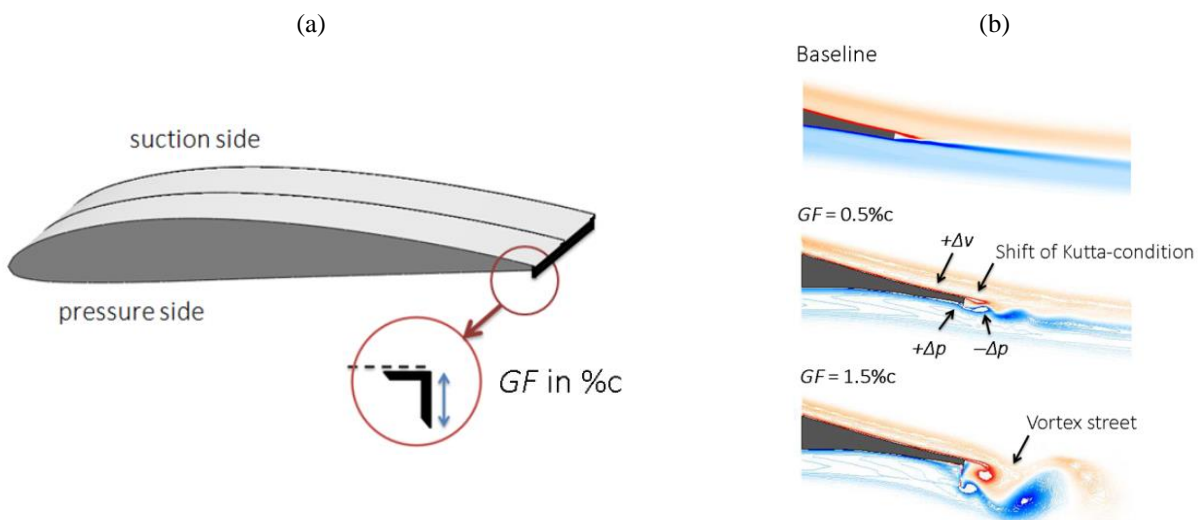
Figure 2. (a) Position of the Gurney flap at the trailing edge of a Clark-Y airfoil section. (b) CFD-simulation of the HQ17 airfoil at
40 Re = 1M, reproduced and modified from Schatz et al. (2004).

2

The research on TE flaps of airplane wings dates back to the early 20th century (Gruschwitz and Schrenk, 1933). The GF itself is named after the racecar driver Dan Gurney, who discovered the significant gain in downforce when applying the device on the rear spoilers of his vehicles. Following from that, GFs have been implemented on certain high lift-dependent transport airliners (Bechert et al., 2000) and helicopter stabilizers (Houghton, 2013). More recently, Vestas® has started offering GFs in combination with Vortex Generators (VGs) as an aerodynamic upgrade of HAWTs, predicting annual yield improvements of up to 2 %. The design of the DTU 10 MW Reference turbine includes smooth wedge-shaped GFs in the first half of the blade length, $0.05R < r < 0.4R$, and with GF-heights in the range of 3.5 %c < GF < 1.3 %c, as reported by Bak et al. (2013).

Figure 2 (b) illustrates the changes in the flow field of the laminar airfoil HQ17 when implementing different GF-heights, as previously reported by Liebeck (1978) based on the Newman airfoil. Key to the aerodynamic understanding is the development of one vortex upstream and two counter-rotating vortices downstream of the GF, as such entailing a low-pressure region in the TE wake. As a result, the downwash angle of the flow becomes steeper, the requirements for pressure recovery on the suction side milder, the local boundary layer thinner and the suction peak higher. Additionally, the flow on the pressure side decelerates leading to a positive pressure built-up in the TE region. The resulting shift in the Kutta-condition is generating increased circulation and thus higher lift, which is one of the main Gurney flap characteristics. At the same time, the low-pressure region aft the TE induces additional drag, especially if vortex shedding is initiated in the form of a Kármán vortex street. Hence, the lift increase is accompanied by a certain drag penalty that affects the Lift-to-Drag (L/D) ratio accordingly.

That is why various experimental and numerical research projects aim to limit the adverse drag increase while maintaining the beneficial lift enhancement of GFs. Giguère et al. (1995) and Kentfield (1996) conclude that the GF-height is supposed to be submerged into the local Boundary Layer (BL) in order to keep the drag on an acceptable level. Bechert et al. (2000) demonstrate that additional holes, slits and especially the pattern of dragonfly wings lead to reduced drag on the HQ17 airfoil at Re = 1M. In addition, promising results are presented for very small GF-heights in the range of 0.2 %c < GF < 0.5 %c, i.e. substantially lower than the BL thickness at the TE. Following from that, CFD-based wake simulations of Schatz et al. (2004) reveal that the amount of induced drag depends on the GF-height, in fact, in a disproportionate manner, illustrated in Figure 2 (b). As such, for GF = 1.5 %c a vortex street is triggered while for GF = 0.5 %c the wake is shed in a relatively smooth way. In a similar manner, Alber et al. (2017) suggest the use of very small GF-heights of approximately half the local BL thickness in order to maintain, or even improve the airfoil L/D-ratio of different DU and NACA airfoils.

The aforementioned design principles are applied on a research turbine using GF-heights of 0.5 %c and 1.0 %c. In addition, forced LE transition is evoked in order to emulate roughness effects. Subsequently, the impact of retrofit GFs is investigated based on the following experiments:

- 3D Ultrasonic Anemometry in the turbine wake to determine the local AoA.

- Pressure taps in the mid-span blade region to determine the local lift performance.

75 • Strain gauges at the blade root to determine the flapwise and the edgewise root bending moments.

In the remaining of this paper, the experimental set-up is described in detail, followed by the presentation and the discussion of the results. The main conclusions are summarized in the final section of this report.

2 Experimental set-up

2.1 Berlin Research Turbine

80 The Berlin Research Turbine (BeRT) is a test bench of the closed-loop wind tunnel of the Hermann-Föttinger Institut at the Technische Universität Berlin. It is a unique wind turbine demonstrator to explore specific fluid-dynamic phenomena based on a fully equipped rotating system, as detailed by Vey et al. (2015).
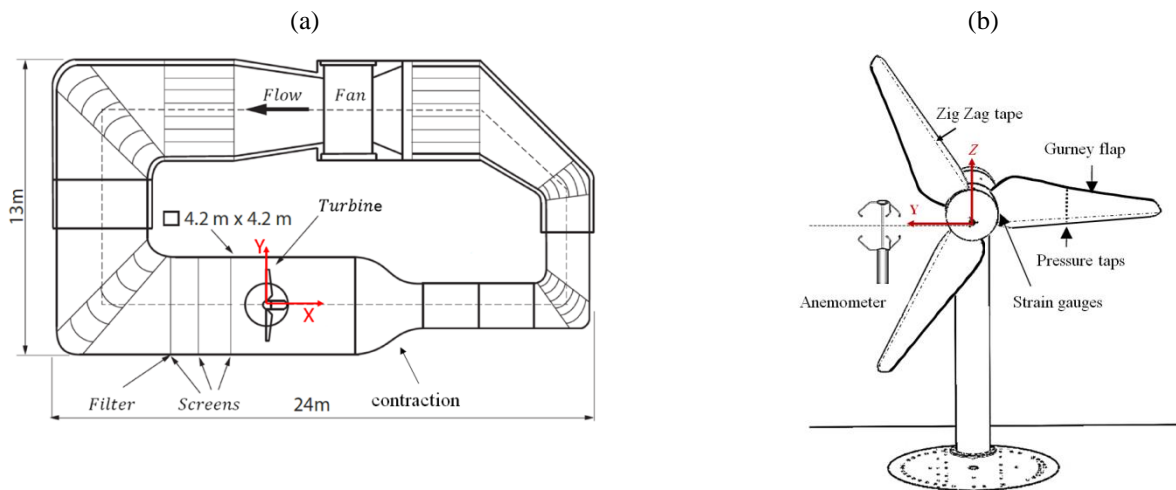
Figure 3. (a) Closed-loop wind tunnel in top-view. (b) BeRT set-up in front-view looking downstream.

Figure 3 (a) depicts the wind tunnel facility consisting of the high speed 2.0 x 1.4 m^2 and the low speed 4.2 x 4.2 m^2 test
85 section. The BeRT is situated in the low speed test section downstream of the flow-conditioning screens and upstream of the wind tunnel contraction. The maximum inflow velocity is 10 ms^{-1}. The third screen upstream the rotor plane is equipped with an additional turbulence filter mat (Vildedon P15/150s) in order to reduce the turbulence intensity to 1.0 % $< Ti <$ 1.5 %, as reported by Bartholomay et al. (2017). Figure 3 (b) displays the BeRT set-up and the measurement methods applied. The rotor radius is R = 1.5 m producing a relatively high blockage ratio of approximately 40 %. Relative distances are expressed
90 in relation to the rotor radius, R, and the zero position at the center of the rotor plane at $X = Y = Z = 0$. The blades consist of the low Reynolds profile Clark-Y with a maximum thickness of th_{max} = 11.9 %c and a modified TE thickness of

th_{TE} = 0.75 %c. The blade geometry is optimized aerodynamically, including a linear decrease of both the chord-length and the twist-angles from root to tip alongside most of the blade length. The root section is contiguous to the round rotor hub and the tip section is pointy, see Figure 4. The tip speed ratio at rated conditions is *TSR* = 4.3 developing a span-wise Reynolds

95 number range from root to tip of 170k < *Re* < 300k. The axial inflow velocity is captured by two parallel Prandtl tubes that are permanently installed at approximately one rotor radius upstream, close to each wind tunnel wall and slightly above hub-height. At rated conditions, the inflow velocity is 6.5 ms^{-1} at a rotational frequency of f_{rot} = 3 Hz. The Data Acquisition (DAQ) system of the rotating sensors, such as pressure taps and strain gauges, is installed within the rotational spinner, displayed in Figure 6 (a). The electrical power is transferred to the rotating system through a slip ring. Communication with

100 the host PC is established via WIFI connection in order to set and modify the rotational speed. The DAQ system captures all channels simultaneously at 10 kHz and streams the data to a host PC via network connection.
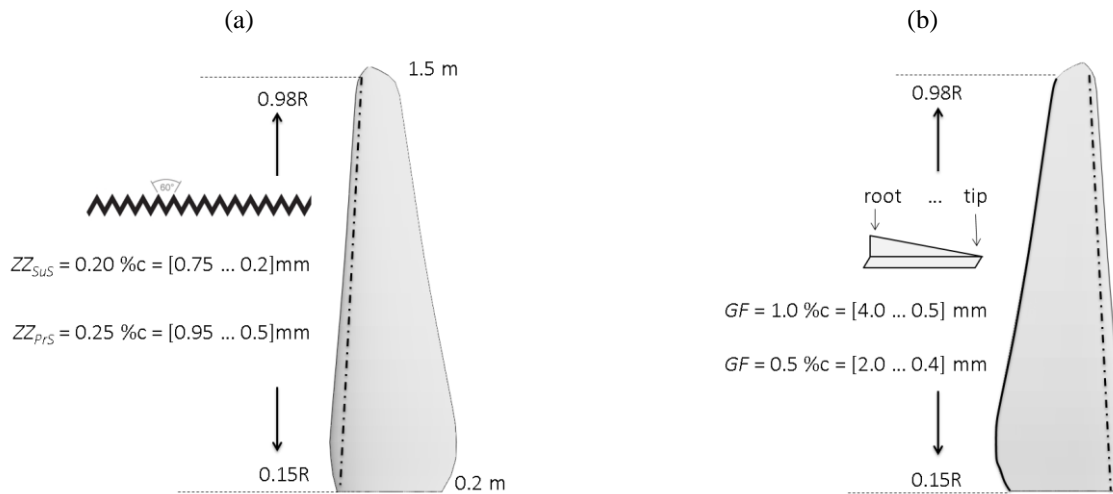
2.2. Blade configurations and operation points

2.2.1 Forced transition

The principal baseline configuration of the BeRT includes Zig Zag (ZZ) turbulator-tape, as established by Klein et al.

105 (2018), in short, the tripped case. ZZ tape is applied in order to initiate the laminar-to-turbulent transition of the Boundary Layer (BL) at a fixed location. In practical terms, it is used to emulate LE roughness-effects on airfoil sections (Rooij and Timmer, 2003) as well as rotor blades (Zhang et al., 2017). Its height is slightly smaller than the local BL thickness in order to trigger the BL transition while avoiding the disproportionate drag increase or even turbulent separation. The ZZ tape is implemented on all BeRT blades at a chord-wise LE position of both the Suction Side (SuS) at x_{SuS} = 5.0 %c and the

110 Pressure Side (PrS) at x_{PrS} = 10.0 %c. The BL thickness of the clean baseline, δ, is calculated with XFOIL, developed by Drela (1989) based on the Reynolds number, the AoA and the N-criterion (Ncrit) modeling the transition location. The design conditions are defined by $α_{opt}$ =5.0°, *Re* = 250k and Ncrit = 6 representing the relatively high *Ti* inside the test section. Depending on δ, the absolute height of the ZZ tape is adjusted in various steps in relation to the chord-length, depicted in Figure 4 (a). For comparative purposes, all experiments are also performed under the consideration of the free BL transition,

115 in short, the clean case, i.e. without including ZZ tape.

2.2.2 Gurney flaps

The GF-height is submerged by the BL at the TE in order to keep the induced drag penalty on an acceptable level. Considering design conditions, XFOIL predicts the BL thickness at the TE to be $δ_{TE}$ = 1.0 %c. In addition, another GF-height of half the local δ is chosen, so that the GF configurations include *GF* = 1.0 %c and *GF* = 0.5 %c. Apart from the very tip

120 section, they are implemented in the form of thin angle profiles made of brass. One side of the angle profiles is cut in a linear way in order to match the linear chord decrease, shown in Figure 4 (b). The other side of the profile is attached with thin double-sided adhesive tape adjacent to the TE.

Figure 4. (a) Zig Zag tape at the leading edge of the suction side. (b) Gurney flap and ZZ tape at the pressure side of the trailing edge.

2.2.3 Test matrix

125 Table 1 summarizes the test matrix that consists of four blade configurations, three Operation Points (OPs) and three measurement methods. The OPs include the so-called stall, rated and feather conditions, which are characterized by low, medium and high TSR or AoA, respectively. Each test run has a total duration of 60 s. The values of both the AoA and the Reynolds numbers refer to the experimental results presented in Sect. 3.

Table 1. Test matrix

Blade configuration		
	Tripped baseline	Clean baseline
$GF = 0.5\,\%c$	Operation points	
$GF = 1.0\,\%c$		
Measurement method		
Ultrasonic anemometry	Wake-velocities → AoA	
Pressure taps	c_p distribution → lift curve	
Strain gauges	Root bending moments	

| Operation point (clean case)			
	Stall	Rated	Feather
TSR	3.0	4.3	5.6
Inflow velocity in ms^{-1}	6.5	6.5	5.0
Rot. frequency in Hz	2.1	3.0	3.0
AoA in ° (Sect. 3.1)	16.5	8.6	4.6
Re-number (Sect. 3.2)	220k	280k	270k

130 **2.3 Measurement methods**

The measurement methods listed in Table 1 consist of three types of sensors that are simultaneously recording the wake velocity, the pressure distribution and the root bending moments.

2.3.1 Ultrasonic anemometry

3D Ultrasonic Anemometers (UAs) are widely spread in the wind energy industry. The technology is recognized by different
135 wind industry standards such as the IEC 61400 to determine the power curve of wind turbines or the Association of German
Engineers (VDI) for turbulence measurements. Moreover, there are numerous references for the use of UAs in the context of
wind tunnel campaigns, such as Weber et al. (1995) and Cuerva et al. (2003). The UA is a commercial product of Thies
CLIMA (version 4.383). According to the manufacturer, they are free from calibration and maintenance.
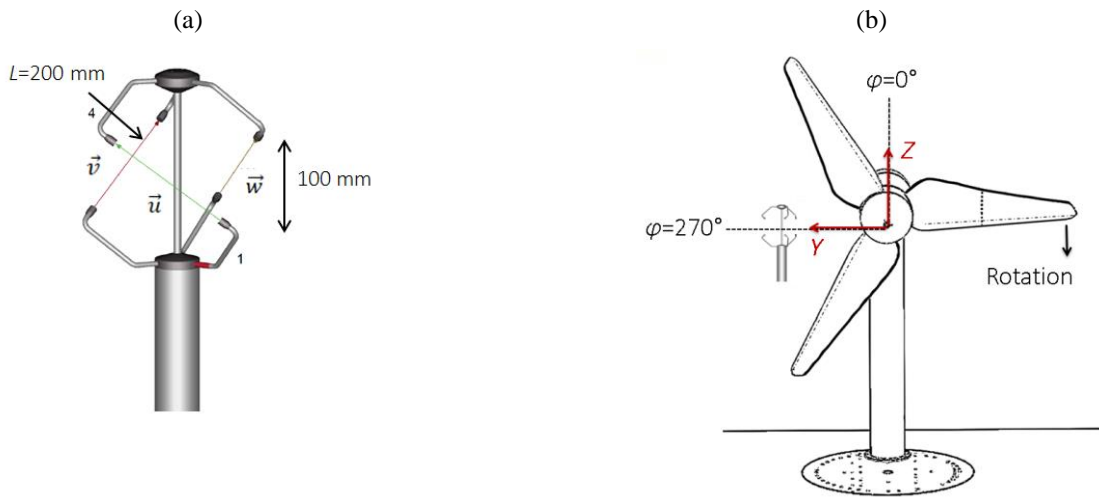
Figure 5. (a) Ultrasonic Anemometer, reproduced and modified from Thies CLIMA. (b) Definition of the azimuthal blade positions
140 looking downstream

Figure 5 (a) displays the three separate acoustic transmitter-receiver pairs that are installed orthogonally to each other. The
velocity vectors, $\vec{u}$, $\vec{v}$ and $\vec{w}$, are determined by six individual measurements based on the bidirectional time-of-flight
principle, i.e. the duration of each signal to be sent and received. They are calculated with

$$\vec{u} = \frac{L}{2}\left(\frac{1}{t_1} - \frac{1}{t_2}\right), \tag{1}$$

145

where $L = 200$ mm is the exact running-length between each sensor pair, so that the measurement volume amounts to
$200 \ x \ 200 \ x \ 200$ mm³. The velocity vectors $\vec{v}$ and $\vec{w}$ are calculated accordingly. Eq. (1) shows that the 3D velocity
calculation depends solely on the average propagation-time of the ultrasound, t_1 and t_2, depending on the specific airflow
passing through the measurement volume. As such, the output values already imply the density and temperature of the air.
150 Subsequently, the velocity vectors are transformed into a natural coordinate system, so that the output time-series consist of
the axial, lateral and vertical velocity components, u, v and w. The device-internal DAQ system is a half-duplex interface
that is completely independent of both the wind tunnel and the BeRT system. According to the manufacturer, the
measurement accuracy is 0.1 ms⁻¹ per value. The data is recorded at a sampling rate of 60 Hz.

Considering the relatively big measurement volume and the relatively low sampling rate compared to e.g. hotwire or laser-based devices, the UA is not adequate for the investigation of complex or high-speed flow structures. However, the BeRT wake-flow is expected to consist of an axial and a tangential velocity component due to the formation of a rotating wake tube. The impact of complex tip and root vortices is considered negligible in the mid-span blade region, as shown by Herráez et al. (2018).

The UA is installed at one static position, i.e. downstream, $X = 1.3R$, in the mid-span region, $Y = 0.56R$, and at hub height, $Z = 0R$, see Figure 5 (b). It is positioned vertically with a spirit level and turned around its own axis towards the axial inflow, so that the lateral and the vertical components, v and w, tend to zero. The set-up is fixed at its final position for all test-runs, which are presented in Sect. 3.

2.3.2 Pressure taps

The pressure distribution is extracted by means of 18 Pressure Taps (PTs) on the SuS and 12 on the PrS, located along the chord-length at $r = 0.45R$, see Figure 6 (b). Each orifice is connected via silicone tubing to its corresponding differential pressure sensor (HCL0025E), i.e. the pressure box inside the spinner. The experimental procedure and the data post-processing is based on Soto-Valle et al. (2019).
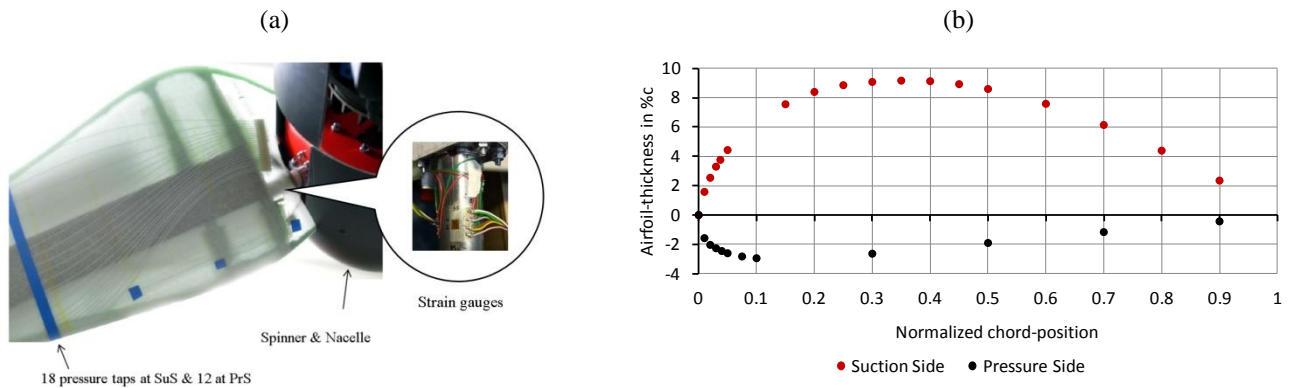
Figure 6. (a) BeRT blade and pressure taps, reproduced and modified from Fischer (2015). (b) Chord-wise position of pressure at $r = 0.45R$.

The differential pressure values are transformed into the pressure coefficient,

$$c_{p,PT} = \frac{\Delta p_{st,PT} + p_{rot}}{p_{dyn,ref}} = \frac{(p_{st,PT} - p_{st,\infty}) + (0.5\rho \cdot (\omega r)^2)}{p_{dyn,ref}}, \qquad (2)$$

where

- $\Delta p_{st,PT}$ is the static pressure difference between each PT and the inflow Prandtl tube $p_{st,\infty}$.

- p_{rot} refers to the pressure due to the rotation of the blade element. It is added to $\Delta p_{st,PT}$ in the form of a constant correction term in accordance with Hand et al. (2001).

- $p_{dyn,ref}$ describes the referential dynamic pressure, i.e. the effective flow velocity experienced by the blade element. Following Hand et al. (2001), it is determined by the maximum pressure that is recorded on the pressure side, the frontal stagnation point, where $c_{p,PT,ref} = 1$. According to Eq. (2) the referential dynamic pressure is then determined by $p_{dyn,ref} = \Delta p_{st,PT,ref} + p_{rot}$.

The c_p valus are phase-averaged over an azimuthal angle of $\varphi = 10°$, shown in Figure 5 (b). Each PT provides a total of 36 pressure values at the following blade positions: $\varphi = [0°, 10°, 20° ... 350°]$, so that $\varphi = 270°$ contains the average of all data points between $265° < \varphi < 275°$.

The pressure difference, Δc_p, is calculated by subtracting the integrated c_p distribution between the PrS and the SuS in order to determine both the normal coefficient, c_n, and the tangential coefficient, c_t. Per definition, $\overrightarrow{c_n}$ is orthogonal to the chord-line pointing towards the SuS, while $\overrightarrow{c_t}$ is parallel to the chord-line pointing towards the LE. According to Hand et al. (2001),

$$c_n = \frac{1}{2} \cdot \sum_{i=1}^{30} \cdot \left(c_{p,PTi} + c_{p,PTi+1} \right) \cdot (x_{PTi+1} - x_{PTi}),$$ (3)

and

$$c_t = \frac{1}{2} \cdot \sum_{i=1}^{30} \cdot \left(c_{p,PTi} + c_{p,PTi+1} \right) \cdot (y_{PTi+1} - y_{PTi}),$$ (4)

where x and y are the normalized chord positions of each PT. The numbering starts at the TE ($x = 0.9$) with the 18 PTs on the SuS until the LE ($x = 0$) and proceeds with the 12 PTs on the PrS from the LE back to the TE.

Subsequently, the lift coefficient, c_l, is determined by

$$c_l = c_n \cdot \cos(\alpha) + c_t \cdot \sin(\alpha).$$ (5)

The required AoA, α, are adopted by the wake measurements of the UAs, see Sect. 3.1. Besides, the term $c_t \cdot \sin(\alpha)$ in Eq. (5) solely describes the pressure drag, i.e. without containing the skin-friction drag, so that $c_t \cdot \sin(\alpha) < c_d$ (Barlow, 1999). Hence, for relatively small AoA, c_t is hardly influencing the lift results that are presented in Sect. 3.

2.3.3 Strain gauges

The Strain Gauges (SGs) are mounted at the clamping of the blade, see Figure 6 (a), in order to detect the Root Bending Moments (RBMs) in the out-of-plane, or flapwise, and in-plane, or edgewise, direction. They are connected in a full-bridge

205 configuration aiming at the mitigation of temperature and cross talk effects. The experimental procedure to determine the RBMs is based on Bartholomay et al. (2018). For the purpose of the comparative investigation between baseline and GF configurations, a simplified post-processing protocol is applied without including the data-based cross talk correction.

Before testing each blade configuration, the offset signal is recorded in slow-motion at the lowest rotating frequency available, $f_{rot} = 0.1$ Hz. In this way, the gravitational RMBs are subtracted from the results, which are otherwise registered as a sinusoidal signal in the edgewise direction. Moreover, at operational frequencies, the axial forces due to the blade rotation

210 are causing a material deformation directed towards the blade tip. They are quantified as a combination of centrifugal and gravitational forces by

$$F_{axial} = F_{cent} - F_{grav} = \left(m_{blade} \cdot r_{cg} \cdot \omega^2 \right) - \left(m_{blade} \cdot g \cdot \cos(\varphi) \right), \qquad (6)$$

where $m_{blade} = 5.67$ kg, the center of gravity is located at $r_{cg} = 0.31R$, g is the gravitational constant and φ refers to each

215 phase-locked blade position. The rotational frequency is kept constant during each test-run, $\omega = $ const, so that the centrifugal force F_{cent} becomes a constant correction term at each OP. The effective flapwise and edgewise RBMs, which are related to the aerodynamic loads acting on the blade, are then determined by

$$M_{flap}(\varphi) = \left(U_{f,raw}(\varphi) - U_{f,off}(\varphi) \right) \cdot K_{f1} - \left(F_{axial} \cdot K_{f2} \right), \qquad (7)$$

$$M_{edge}(\varphi) = \left(U_{e,raw}(\varphi) - U_{e,off}(\varphi) \right) \cdot K_{e1} - \left(F_{axial} \cdot K_{e2} \right), \qquad (8)$$

220

where

- M_{flap} and M_{edge} are the aerodynamic flapwise or edgewise RBMs in Nm.
- $U_{f,raw}$ and $U_{e,raw}$ stand for the raw data signal in V.
- $U_{f,off}$ and $U_{e,off}$ describe the slow-motion offset signal in V.

225
- K_{f1} and K_{e1} refer to constant calibration factors to transform V into Nm.
- K_{f2} and K_{e2} refer to constant calibration factors to transform the axial forces from N into Nm.

Applying Eq. (7) and (8) both the out-of-plane and the in-plane RBMs are computed for each of the 36 blade positions, presented in Sect. 3, as follows.

3 Results

The results of both the tripped and the clean cases are presented and discussed. For space economy, the clean case is only included in terms of the concluding results, i.e. the lift performance in Sect. 3.2 and the root bending moments in Sect. 3.3, but otherwise accessible in Appendix A for completeness.

3.1 Wake velocities and angles-of-attack

Simultaneously to the inflow Prandtl tubes, the 3D wake velocities are recorded with the UA at one static position at hub-height, downstream and in the mid-span blade area, see Figure 5 (b).

(a)   (b)
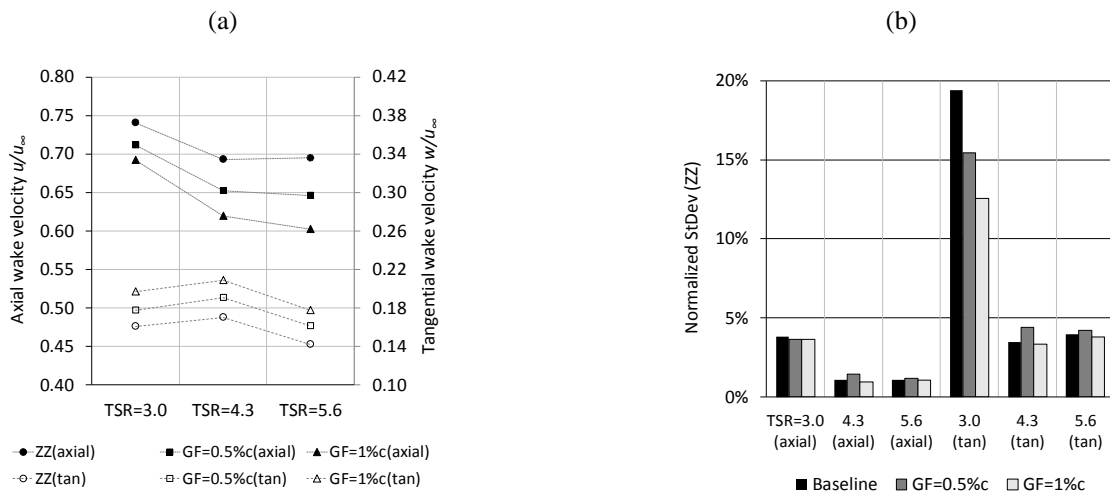
Figure 7. Tripped case. (a) Axial and tangential wake velocities normalized by the inflow velocity. (b) Standard deviation of the wake velocities normalized by the average wake velocities.

Starting from the baseline, the axial wake velocities depicted in Figure 7 (a) are found significantly higher compared to typical far field conditions. According to the steady state BEM, the optimum axial wake velocity is supposed to be around one third of the inflow (Burton, 2011). In this case, it amounts to more than two thirds at rated conditions. This phenomenon is caused by the wind tunnel blockage effects, as shown via URANS simulations using the fluid dynamic code FLOWer. At rated conditions of the BeRT, Klein et al. (2018) predict that the flow decelerates to an axial wake velocity in the range of $0.62\,u_\infty < u_{CFD} < 0.77 u_\infty$, which is in agreement with the experimental results, $u_{EXP} = 0.69 u_\infty$. Furthermore, the corresponding tangential velocity is similar to the steady state BEM simulation of QBlade (Marten et al., 2013) based on the XFOIL settings (Sect. 2.2.1) with $w_{BEM} = 0.18 u_\infty$ and $w_{EXP} = 0.17 u_\infty$. Hence, the tangential wake velocity is relatively close to the standard BEM simulation, despite the influence of the wind tunnel walls.

Regarding the impact of the GFs, Figure 7 (a) illustrates the consistent decrease of the axial, and the consistent increase of the tangential wake velocity both in relation to the GF-height. The lateral velocity component is neglected as it amounts to $v << \pm 0.1$ ms^{-1}. Moreover, Figure 7 (b) summarizes the standard deviation normalized by the corresponding average velocity

component, thus expressed in percent. Primarily, it depends on the OP showing significantly higher values under stall conditions. Hence, the flow separation is captured by the UA in the form of a more turbulent wake field, especially in terms of the tangential component. The GF configurations do not influence the wake turbulence considerably, except for the tangential velocity component at stall, $TSR = 3.0$, where the GFs appear to mitigate the turbulence level.

255

Next, the wake velocity is expressed by the axial and tangential rotor induction factors, a and a', in order to determine the local AoA and to quantify the results. Following Burton (2011), the induction factors are defined by

$$a = \frac{1}{2}\left(1 - \frac{u}{u_\infty}\right),$$ (9)

and

$$a' = \frac{w}{2\omega r}.$$ (10)

260 The induction factors, a and a', describe the decrease of the axial, and the increase of the tangential velocity component from a reference point sufficiently far away from the rotor plane (Snel et al., 2009). In this case, the measurements are taken at a distance of $X = 1.3R$ downstream the rotor in order to avoid the influence of the wind tunnel contraction, see Figure 3 (a). According to Hansen (2015) and Eq. (9) and (10), the AoA, α, is calculated by the following trigonometric operation,

$$\alpha = \arctan\left(\frac{(1-a)\,u_\infty}{(1+a')\,\omega r}\right) - \beta = \arctan\left(\frac{u_\infty+u}{2\omega r+w}\right) - \beta,$$ (11)

265

where the twist-angle at the radial location of the UA is $\beta\,(0.56R) = 9.8°$.
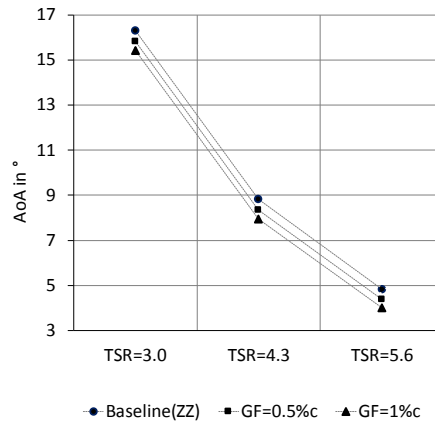

Figure 8. Angles-of-attack in the tripped case.

At rated conditions and considering the horizontal blade position, $\varphi = 270°$, the AoA of the baseline case amount to
270   $\alpha_{ZZ} = 8.8°$, see Figure 8. This outcome is in agreement with comparable investigations in the mid-span region based on
3-hole probes as well as URANS simulations, as detailed by Klein et al. (2018). Furthermore, Figure 8 displays the
consistent AoA-decrease caused by the GF configurations. Depending on the GF-height, it amounts to $\Delta\alpha_{GF=0.5\%c} = 0.5°$ and
$\Delta\alpha_{GF=1.0\%c} = 0.9°$, i.e. to a more favorable level. As such, the results quantify one of the crucial effects of retrofitted GFs on
the blade performance; decreasing axial wake velocities and thus smaller AoA. In the following Sect. 3.2, the changing AoA
275   are correlated to the local lift coefficients in the mid-span blade region.

3.2 Pressure distribution and lift performance
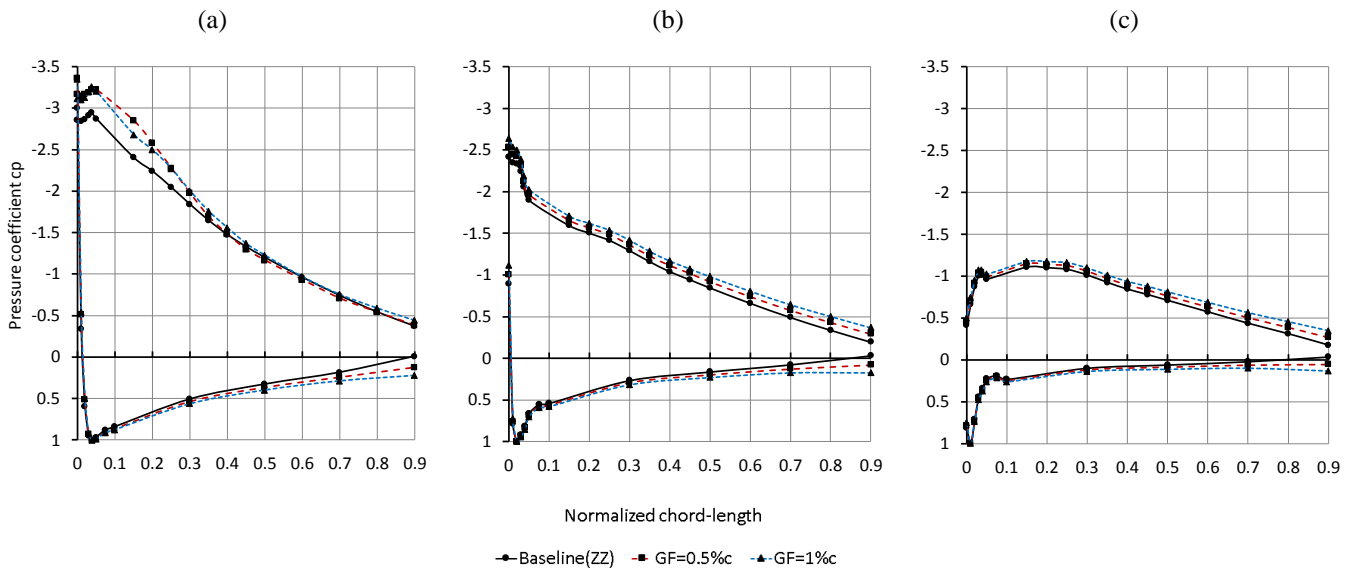
Figure 9. Pressure distribution in the tripped case at $\varphi = 270°$. (a) $TSR = 3.0$. (b) $TSR = 4.3$. (c) $TSR = 5.6$.

Figure 9 visualizes the c_p distribution at $r = 0.45R$ at the horizontal blade position. Depending on the OP, Δc_p expands along
the complete chord-length when applying GFs. This effect is particularly visible in terms of the aft-loading towards the TE at
280   $0.7 < x < 0.9$. In fact, the aft-loading tail is one of the main design approaches in order to improve the roughness sensitivity
of the DU airfoils (Rooij and Timmer, 2003). At stall, $TSR = 3.0$, the separation at the SuS is not complete, despite the
elevated AoA, $\alpha_{ZZ} = 16.3°$. Compared to the XFOIL simulations (Sect. 2.3.1), the maximum lift coefficient of the Clark-Y
airfoil is reached at $c_{l,max} \approx 14.0°$. Hence, the c_p curves seen in Figure 9 (a) indicate the effect of stall delay due to the blade
rotation, as discussed hereafter. In order to quantify the results, the c_p distribution is transformed into the local lift curve
285   based on Eq. (5). The required AoA are adopted from Sect. 3.1, so that the lift coefficients combine both the wake-velocity
and the pressure measurements.
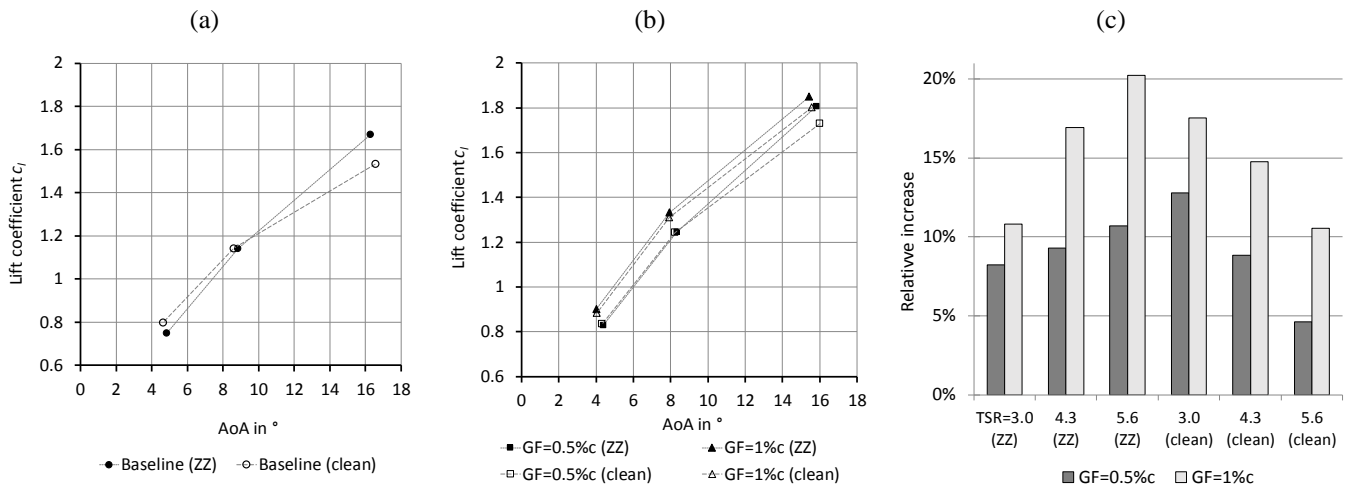
Figure 10. Lift coefficients over angle-of-attack in tripped and clean cases. (a) Baseline configurations. (b) Gurney flap configurations. (c) Relative lift increase of Gurney flap configurations in relation to the corresponding baseline.

290 Figure 10 (a) compares the lift coefficients between the tripped and the clean cases. In the pre-stall region, $4° < \alpha < 5°$, the tripped case shows smaller lift coefficients due to the forced BL transition at the LE. At higher AoA, $8° < \alpha < 9°$, this is not the case anymore, while in the stall region, $15° < \alpha < 17°$, the ZZ tape appears to develop a beneficial effect on the lift performance. This phenomenon is probably caused by the tripped BL that remains attached until closer to the TE. In the clean case, however, the less energetic BL separates earlier thus leading to smaller lift coefficients at higher AoA. In general,

295 ZZ tape evoking a smoother stall behavior is found by comparable wind tunnel conditions, such as Holst et al. (2016) based on the FX 63-137 airfoil section at Re = 200k using ZZ tape with a thickness of 0.75 mm. Despite the decrease in the pre-stall, the lift coefficients are found on a similar level in the post-stall region.

Figure 10 (b) compares the lift coefficients between the tripped and the clean GF configurations. The lift performance in the tripped case is on a similar, or even higher level considering the complete AoA range, $4° < \alpha < 17°$. Hence, forced LE

300 transition is not mitigating or neutralizing the GF effect on the lift performance. On the contrary, the results indicate that the GF configurations are alleviating the adverse effects of LE roughness.

Furthermore, Figure 10 (c) summarizes the relative lift increase of both GF configurations in relation to the corresponding baseline cases. On the one hand, the benefit for the clean case is greater at stall, TSR = 3.0, where the blade is underperforming compared to the tripped BL, as discussed. On the other hand, the relative lift increase in the tripped case is

305 greater considering the pre-stall region, TSR = 5.6, where the adverse effect of the ZZ tape is more pronounced. At rated conditions, TSR = 4.3, the differences with respect to the tripped baseline amount to $\Delta c_{l,GF=0.5\%c}$ = 0.11 (9.3 %) and $\Delta c_{l,GF=1.0\%c}$ = 0.19 (16.9 %), as such illustrating the main characteristic of retrofit GFs; the considerable increase of lift.

Moreover, the scale of Δc_l is in agreement with comparable wind tunnel experiment based on a similar Clark-Y airfoil section, as depicted in Figure 11.
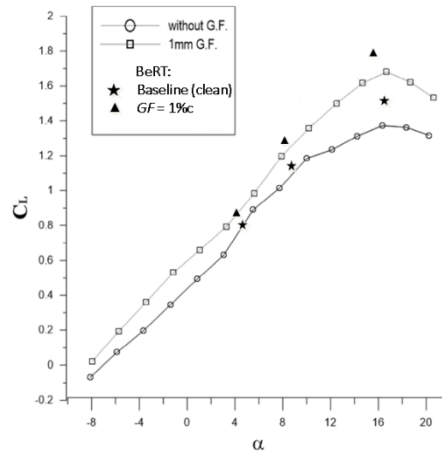
Figure 11. Lift coefficients of a Clark-Y airfoil including Gurney flap, reproduced and modified from Kheir-Aldeen (2014).

Figure 11 compares the lift coefficients of the clean Clark-Y airfoil section (th_{max} = 14.0 %c, Re = 210k, GF = 1.2 %c) and the clean Clark-Y blade element of the BeRT (th_{max} = 11.9 %c, Re = 280k, GF = 1.0 %c). The results demonstrate close similarities for both the baseline and the GF configurations. The slightly elevated lift values in case of the BeRT are due to the thinner Clark-Y blade element. At $c_{l,max}$, the blade performance is furthermore characterized by the radial flow due to the blade rotation causing stall delay. This behavior is in agreement with experiments on the field rotor at the Delft University of Technology. Rooij and Timmer (2003) report a shift of $c_{l,max}$ by several degrees compared to 2D airfoil simulations. After evaluating one area of the mid-span blade region, Sect. 3.3 is presenting the impact of GFs over the complete blade span.
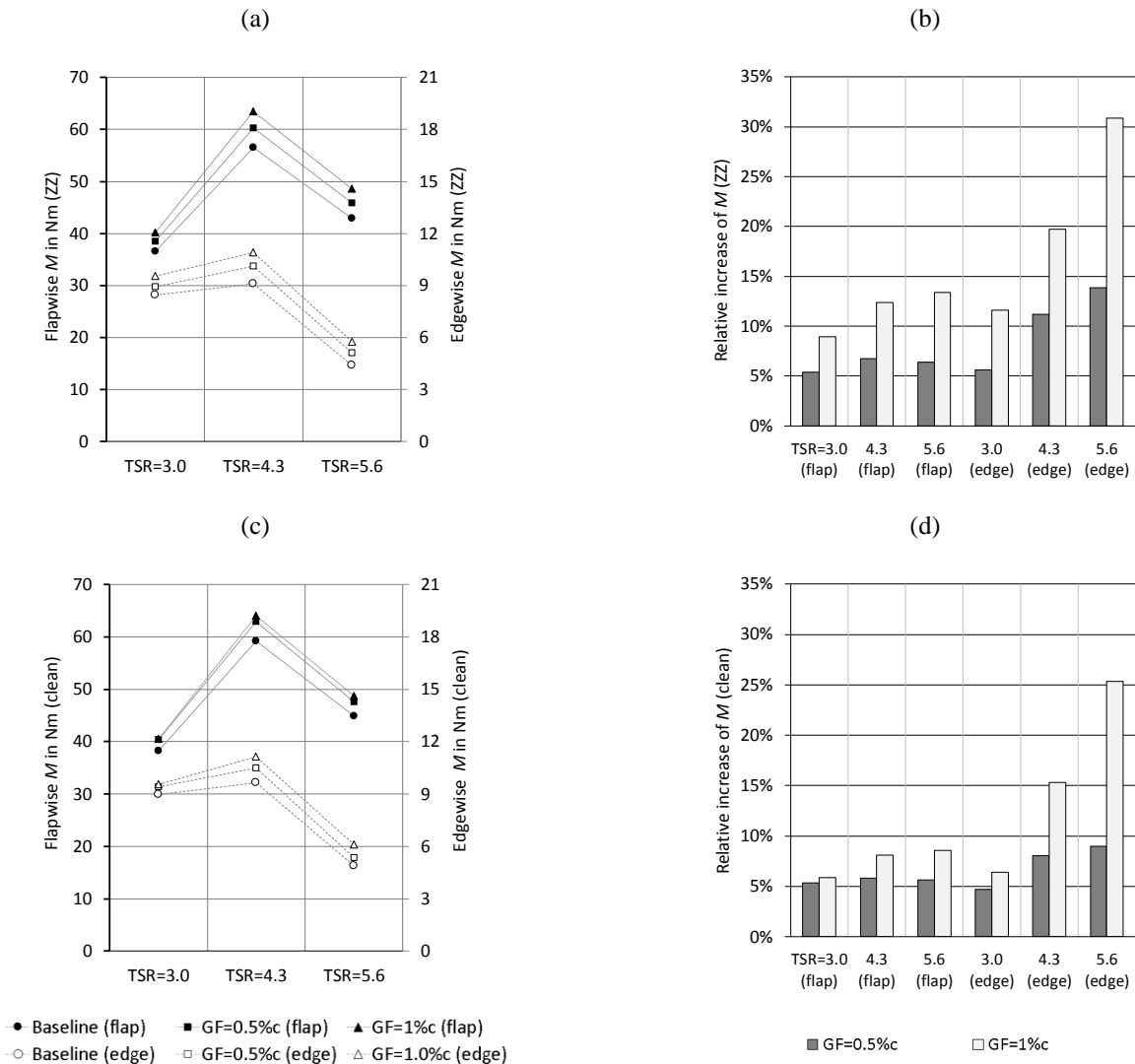
3.3 Root bending moments
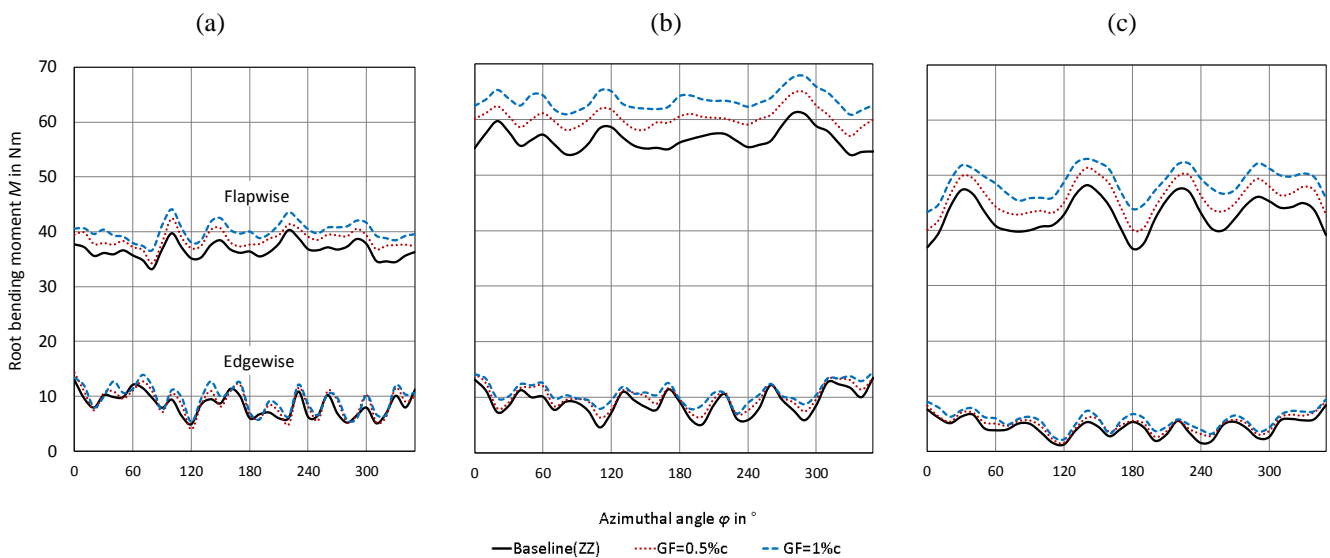
Figure 12. Flapwise and edgewise root bending moments in the tripped case. (a) TSR = 3.0. (b) TSR = 4.3. (c) TSR = 5.6.

15

The integration of the aerodynamic loads, i.e. the lift and the drag forces acting along the blade span, yield the RBMs. The in-plane or edgewise RBMs are proportional to the rotor torque and thus the mechanical power output. They are directly related to the out-of-plane or flapwise RBMs, which are proportional to the rotor thrust, i.e. the structural loads (Hansen, 2015).

325

The aerodynamic RBMs are recorded over one blade revolution, i.e. over all 36 phase-locked blade positions, displayed in Figure 12. The impact of the GF configurations is registered as a consistent increase of both the flapwise and the edgewise RBMs. In order to quantify the results, the RBMs are presented as average values for both the tripped and the clean cases.

Figure 13. Flapwise and edgewise root bending moments. (a) Tripped case. (b) Relative increase to tripped baseline. (c) Clean case. (d) Relative increase to clean baseline.

330

16

The results of Figure 13 (a) confirm the increment of the RMBs in relation to the GF-height in accordance with Figure 12. In the clean case, the overall trend is similar to the tripped case considering all OPs, see Figure 13 (c). This means that the impact of Gurney flaps, previously quantified in terms of the local lift coefficients, is now registered in the form of increased RBMs in both the flapwise and the edgewise direction.

335

In Figure 13 (b), the performance of the GF configurations is quantified in relation to the tripped baseline. At rated conditions, the average increase of the flapwise RBMs amount to $\Delta M_{\mathrm{flap,GF=0.5\%c}}$ = 3.8 Nm (6.7 %) and to $\Delta M_{\mathrm{flap,GF=1.0\%c}}$ = 7.0 Nm (12.4 %). At the same time, the edgewise RBMs are enhanced by $\Delta M_{\mathrm{edge,GF=0.5\%c}}$ = 1.0 Nm (11.2 %) and $\Delta M_{\mathrm{edge,GF=1.0\%c}}$ = 1.8 Nm (19.7 %). In the clean case, see Figure 12 (d), the overall trend is similar, however less

340 pronounced considering the complete range of OPs. Hence, in both cases, the GF configurations evoke performance improvements regarding the rotor torque, however at the expense of the inherent increase of the rotor thrust.

Furthermore, the results reinforce the observation that the impact of GFs is more profound in relation to the tripped, rather than the clean baseline. Hence, comparing the relative increase between Figure 13 (b) and (d), the GF configurations are

345 alleviating the effects of forced LE transition, especially on the edgewise RBMs, as previously discussed in Sect. 3.2 with respect to the local lift performance.

4 Conclusions

The aerodynamic impact of Gurney flaps is investigated on the rotor blades of the so-called Berlin Research Turbine. The baseline measurements confirm the influence of the prevailing wind tunnel blockage effects. At rated conditions and in the

350 mid-span blade region, the axial wake velocity is approximately double in comparison to ideal far field conditions. As such, the corresponding angles-of-attack are elevated in comparison to the design case and amount to α_{exp} = 8.8°, rather than α_{opt} = 5.0°.

In this situation, the retrofit application of Gurney flaps is leading to performance improvements considering both the tripped and the clean cases, including tip speed ratios of 3.0, 4.3 and 5.6. At rated conditions, TSR = 4.3, the axial wake velocities

355 are decreased and the angles-of-attack are reduced by $\Delta\alpha_{GF=0.5\%c}$ = 0.5° and $\Delta\alpha_{GF=1.0\%c}$ = 0.9°. At the same time, the local lift coefficients are enhanced by $\Delta c_{l,GF=0.5\%c}$ = 0.11 (9.3 %) and $\Delta c_{l,GF=1.0\%c}$ = 0.19 (16.9 %), which is the main characteristics of Gurney flaps. The effect of the aerodynamic loads over the complete blade span is analyzed in terms of the root bending moments. The average increase in the out-of-plane direction amounts to $\Delta M_{\mathrm{flap,GF=0.5\%c}}$ = 3.8 Nm (6.7 %) and to $\Delta M_{\mathrm{flap,GF=1.0\%c}}$ = 7.0 Nm (12.4 %). Simultaneously, the in-plane bending moments are enhanced by

360 $\Delta M_{\mathrm{edge,GF=0.5\%c}}$ = 1.0 Nm (11.2 %) and $\Delta M_{\mathrm{edge,GF=1.0\%c}}$ = 1.8 Nm (19.7 %). Hence, decreasing angles-of-attack and increasing lift coefficients are correlated with the enhancement of both the rotor torque and the thrust. Furthermore, the aerodynamic

impact of Gurney flaps is found more pronounced in the tripped case compared to the clean case. This observation indicates the capacity of the Gurney flap configurations to alleviate the adverse effects of forced LE transition.

365 In summary, Gurney flaps are considered a worthwhile passive flow-control device for the use on horizontal axis wind turbines. The retrofit application is a useful option for the inner blade region in order to alleviate the adverse effects of flow separation due to elevated angles-of-attack. Another promising application of Gurney flaps is the compensation of leading edge roughness due to surface erosion throughout large parts of the blade span. However, the design of the Gurney flap-height is crucial in order to avoid negative aerodynamic effects, such as induced drag due to additional vortex shedding.

370 Further research is required quantifying the impact of different Gurney flap configurations on the dynamic loads and the overall energy yield of wind turbines.

Appendix A: Results of the clean case
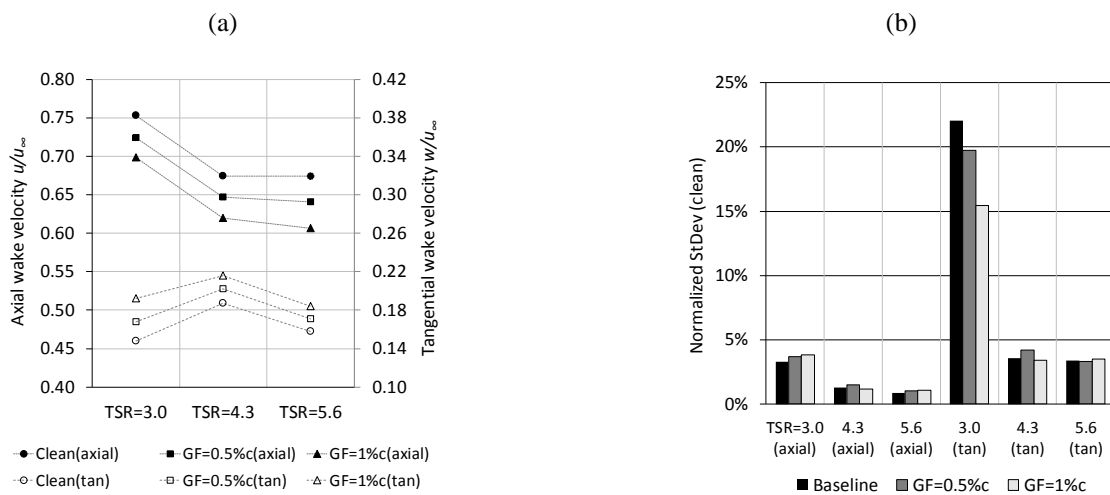
Figure A 1. Clean case. (a) Axial and tangential wake velocities normalized by the inflow velocity. (b) Standard deviation of the wake velocities normalized by the average wake velocities.
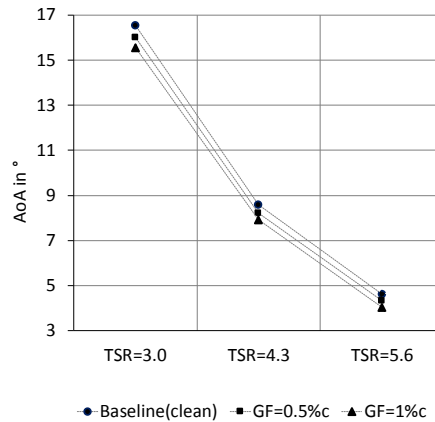
375
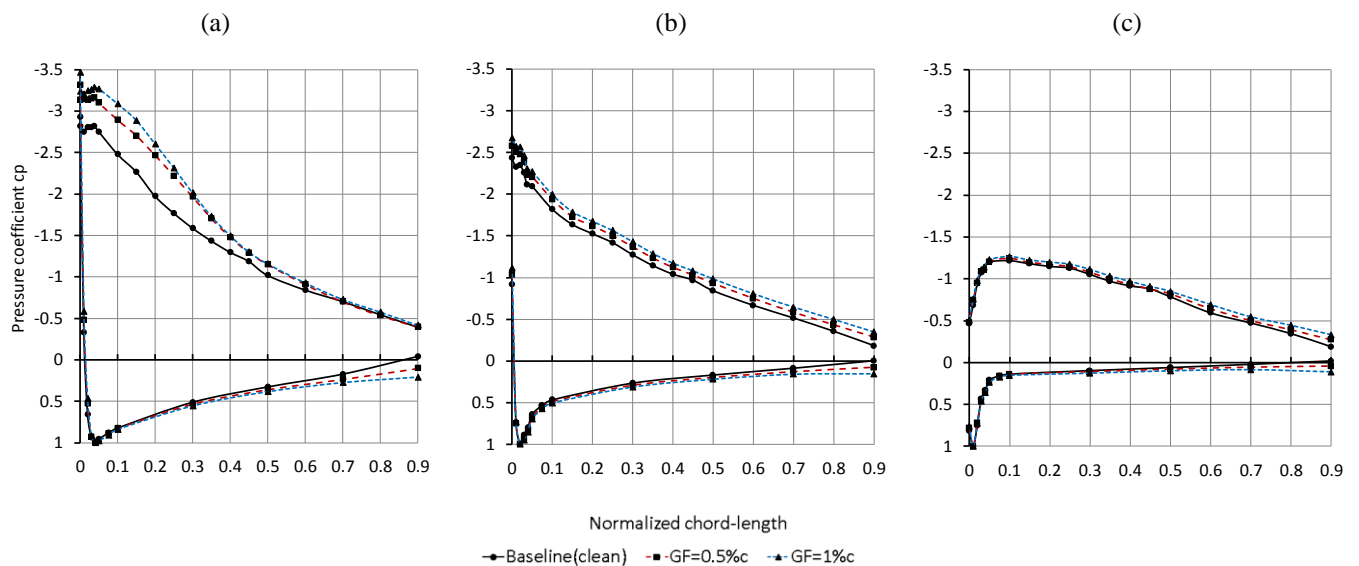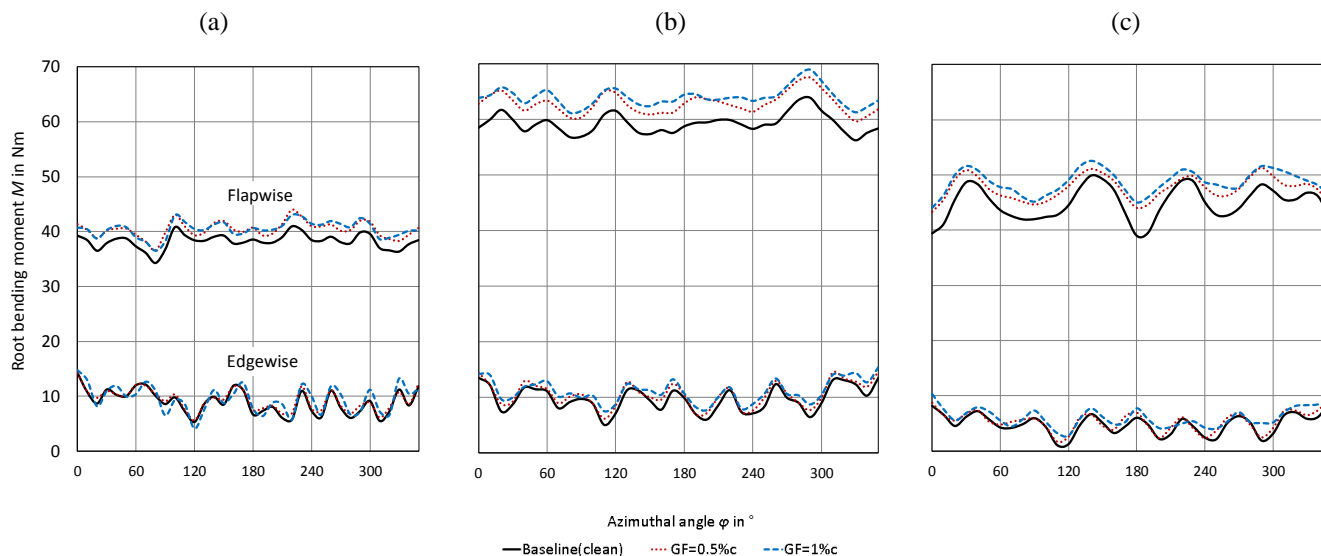
Figure A 2. Angles-of-attack in the clean case.

Figure A 3. Pressure distribution in the clean case at $\varphi = 270°$. (a) $TSR = 3.0$. (b) $TSR = 4.3$. (c) $TSR = 5.6$.

Figure A 4. Flapwise and edgewise root bending moments in the clean case. (a) *TSR* = 3.0. (b) *TSR* = 4.3. (c) *TSR* = 5.6.

Data availability.

Measurement data and results can be provided by contacting the corresponding author.

Author contribution

Jörg Alber performed the wind tunnel experiments together with Rodrigo Soto-Valle and the support of all co-authors. Jörg Alber processed the data and prepared the manuscript with the support of Marinos Manolesos and Rodrigo Soto-Valle both of whom contributed with important comments and suggestions to all section of the manuscript.

Competing interests

The authors declare that they have no conflict of interest.

References

Alber, J., Pechlivanoglou, G., Paschereit, C. O., Twele, J. and Weinzierl, G.: Parametric Investigation of Gurney Flaps for
the Use on Wind Turbine Blades, ASME Turbo Expo, https://doi.org/10.1115/GT2017-64475, 2017.

Bak, C., Zahle, F., Bitsche, R., Kim, T., Yde, A., Henriksen, L.C., Natarajan, A., and Hansen, M.: Description of the DTU
10 MW Reference Wind Turbine, Technical University of Denmark, DTU Wind Energy, 2013.

Barlow, J. B., Rae, W. H., Pope, A.: Low-Speed Wind Tunnel Testing, John Wiley & Sons, 3rd edition, USA, 1999.

Bartholomay, S., Fruck, W. L., Pechlivanoglou, G., Nayeri, C. N. and Paschereit, C. O.: Reproducible Inflow
Modifications for a Wind Tunnel Mounted Research HAWT, ASME Turbo Expo, https://doi.org/10.1115/GT2017-
64364, 2017.

Bartholomay, S., Marten, D., Martínez, M. S., Alber, J., Pechlivanoglou, G., Nayeri, C. N., Paschereit, C. O., Klein, A. C.,
Lutz, T., and Krämer, E.: Cross-Talk Compensation for Blade Root Flap- and Edgewise Moments on an
Experimental Research Wind Turbine and Comparison to Numerical Results, ASME Turbo Expo,
https://doi.org/10.1115/GT2018-76977, 2018.

Bechert, D. W., Meyer, R. and Hage, W.: Drag reduction of airfoils with miniflaps - Can we learn from dragonflies?,
AIAA Paper, https://doi.org/10.2514/6.2000-2315, 2000.

Burton, T., Jenkins, N., Sharpe, D. and Bossanyi, E.: Wind Energy Handbook, 2nd edition, Wiley Interscience, UK, 2011.

Cuerva, A., Tejero, Sanz-Andrés, A. and Navarro, J.: On multiple-path sonic anemometer measurement theory, Exp.
Fluids, Bd. 34, S. 345–357, https://doi.org/10.1007/s00348-002-0565-x., 2003.

Drela, M.: XFOIL: An Analysis and Design System for Low Reynolds Number Airfoils, MIT: Massachusetts Institute of
Technology, https://doi.org/10.1007/978-3-642-84010-4_1, 1989.

Fischer, J.: BWKA-1.5 TUB - Blades with Servo controlled Flaps, Smart Blade ®, Berlin, Germany, 2015.

Giguére, P., Lemayt, J. and Dumas, G.: Gurney flap effects and scaling for low-speed airfoils, AIAA Paper,
https://doi.org/10.2514/6.1995-1881, 1995.

Gruschwitz, E. and Schrenk, O.: A simple method for increasing the lift of airplane wings by means of flaps, Zeitschrift fuer
Fluegtechnik und Motorluftschiffahrt, Vol 23 No 20, 1933.

Hand, M., Simms, D., Fingersh, L., Jager, D., Cotrell, J., Schreck, S. and Larwood, S.: Unsteady aerodynamics experiment
phase VI: wind tunnel test configurations and available data campaigns, National Renewable Energy Lab,
DOI:10.2172/15000240, 2001.

Hansen, M. O. L.: Aerodynamics of Wind Turbines, 2nd Edition, Earthscan, UK, 2015.

Herráez, I., Daniele, E. and Schepers, J. G.: Extraction of the wake induction and angle of attack on rotating wind turbine
blades from PIV and CFD results, Wind Energy Science, https://doi.org/10.5194/wes-3-1-2018, 2018.

Holst, D., Pechlivanoglou, G., Kohlrausch, C. T., Nayeri, C. N. and Paschereit, C. O.: sHAWT Design: Airfoil

425   Aerodynamics Under the Influence of Roughness, ASME Turbo Expo, https://doi.org/10.1115/GT2016-56377, 2016.

Houghton, E. L.: Aerodynamics for Engineering Students, Aerodynamics for Engineering Students, 2013.

Kentfield, J.: The Influence of Free-Stream Turbulence Intensity on the Performance of Gurney-Flap Equipped Wind-Turbine Blades, Wind Engineering, https://www.jstor.org/stable/43749607, 1996.

430   Kheir-aldeen, M., and Hamid, A.: Experimental Study to the Effect of Gurney Flap on the Clark Y-14 Airfoil Wing Model, International Journal of Innovation and Scientific Research, ISSN 2351-8014, 2014

Klein, A. C., Bartholomay, S., Marten, D., Lutz, T., Pechlivanoglou, G., Nayeri, C. N., Paschereit, C. O., and Krämer, E. About the suitability of different numerical methods to reproduce model wind turbine measurements in a wind tunnel with a high blockage ratio, Wind Energy Science, https://doi.org/10.5194/wes-3-439-2018, 2018.

435   Liebeck, R. H.: Design of subsonic airfoils for high lift, Journal of Aircraft, https://doi.org/10.2514/3.58406, 1978.

Marten, D, Wendler, J., Pechlivanoglou, G., Nayeri, C. N. and Paschereit, C. O.: Development and Application of a Simulation Tool for Vertical and Horizontal Axis Wind Turbines, ASME Turbo Expo, https://doi.org/10.1115/GT2013-94979, 2013.

Pechlivanoglou, G., Fuehr, S., Nayeri, C. N. and Paschereit, C. O.: The Effect of Distributed Roughness on the Power
440   Performance of Wind Turbines, ASME Turbo Expo, https://doi.org/10.1115/GT2010-23258, 2010.

Pechlivanoglou, G., Philippidis T. P., Vey, S., Eisele, O., Nayeri, C. N. and Paschereit, C. O.: Vortex Generators for Wind Turbine Blades: Wind Tunnel Tests, Field Simulations and Structural Analysis, ASME Turbo Expo, RZGM2013-34, 2013.

Rooij, R P.J.O.M. van and Timmer, W. A.: Roughness Sensitivity Considerations for Thick Rotor Blade Airfoils, AIAA
445   Paper 2003-0350, https://doi.org/10.2514/6.2003-350, 2003.

Schatz, M., Günther, B., and Thiele, F. Computational modeling of the unsteady wake behind Gurney-flaps, AIAA Paper, https://doi.org/10.2514/6.2004-2417, 2004.

Snel, H., Schepers, J. G., and Siccama, N. B.: Mexico project: The database and results of data processing and interpretation, AIAA Paper, https://doi.org/10.2514/6.2009-1217, 2009.

450   Soto-Valle, R., Bartholomay, S., Alber, J., Manolesos, M., Nayeri, C. N., Paschereit, C. O.: Determining the Angle of Attack along a Wind Turbine Rotor Blade in Wind Tunnel Experiments, Wind Energy Science, https://doi.org/10.5194/wes-2020-35, 2020.

Vey, S., Marten, D., Pechlivanoglou, G., Nayeri, C. and Paschereit, C. O.: Experimental and Numerical Investigations of a Small Research Wind Turbine, AIAA Paper, https://doi.org/10.2514/6.2015-3392, 2015.

455   Weber, F.I., Durgin, W. W. and Iohari, H.: Circulation measurements about a rapidly pitching airfoil using an ultrasonic system, AIAA Paper, https://doi.org/10.2514/6.1995-2269, 1995.

Wilcox, B. J., White, E. B. and Maniaci, D. C.: Roughness Sensitivity Comparisons of Wind Turbine Blade Sections, SANDIA REPORT, SAND2017-11288, DOI:10.2172/1404826, 2017.

Zhang, Y., van Zuijlen, A. and van Bussel, G.: The MEXICO rotor aerodynamic loads prediction: ZigZag tape effects and

460   laminar-turbulent transition modeling in CFD, Journal of Wind Engineering and Industrial Aerodynamics, https://doi.org/10.1016/j.jweia.2017.06.002, 2017.